Accuracy assessment of fringe projection profilometry and digital image correlation techniques for three-dimensional shape measurements

Journal of Physics: Photonics

OPEN ACCESS

RECEIVED
28 August 2020

REVISED
26 October 2020

ACCEPTED FOR PUBLICATION
18 November 2020

PUBLISHED
5 January 2021

PAPER

Accuracy assessment of fringe projection profilometry and digital image correlation techniques for three-dimensional shape measurements

Hieu Nguyen[1,2], **Jiali Liang**[3], **Yuzeng Wang**[4] **and Zhaoyang Wang**[2]

[1] Neuroimaging Research Branch, National Institute on Drug Abuse, National Institutes of Health, Baltimore, MD 21224, United States of America
[2] Department of Mechanical Engineering, The Catholic University of America, Washington, DC 20064, United States of America
[3] Department of Astronomy, The University of Maryland, College Park, MD 20742, United States of America
[4] School of Mechanical Engineering, Jinan University, Jinan 250022, People's Republic of China

E-mail: wangz@cua.edu

Keywords: three-dimensional image acquisition, three-dimensional sensing, three-dimensional shape reconstruction, depth measurement, structured light; fringe projection profilometry, digital image correlation

Abstract

With ever-increasing demand for three-dimensional (3D) imaging and shape measurements in a variety of fields, measurement accuracy has become of vital importance to numerous scientific and engineering applications. This paper presents an experimental investigation into the accuracy comparison of two prevalent 3D imaging and shape measurement methods: fringe projection profilometry (FPP) and 3D digital image correlation (3D-DIC) techniques. A detailed description of their principles reveals their inherent similarities and fundamental differences. A measurement system composed of both techniques is employed in the study, and a test target with speckle checkerboard patterns on its surface is adopted to allow simultaneous FPP and 3D-DIC measurements. The evaluation puts emphasis on how the geometric angles between key hardware components affect the 3D measurement accuracy. Experiments show that the depth and height measurements of both techniques can reach sub-micron accuracy, and the relative accuracy of the 3D shape or position measurements can reach 1/600 000.

1. Introduction

In the past two decades, three-dimensional (3D) imaging and shape measurement technology has made remarkable progress and become a popular subject of interest in scientific research and engineering applications. The impact of the 3D imaging and shape measurement can be seen in numerous fields, such as machine vision, medical practice, reserve engineering, quality assurance, biometric security, 3D printing, entertainment, and unmanned transportation [1–10]. There are many key features to characterize the performance of a 3D imaging and shape measurement technique, including speed, resolution, accuracy, reliability, cost, application scenario, etc. Although there are often trade-offs among these features, measurement accuracy is always an essential one in the applications of the 3D imaging and shape measurement technology. The accuracy is related to several factors, including but not limited to technical mechanism, system components and setup, field of view, system calibration, geometric and surface characteristics of the measured objects, and ambient illumination. Accordingly, striving for a 3D imaging and shape measurement system with the most possible accurate performance has posed a difficult technical challenge.

Typical non-contact 3D imaging techniques for shape and deformation measurements include: the time-of-flight (TOF) method, interferometry method, laser scanning method, photogrammetry method, moiré method, structured-light or fringe projection method, stereo vision method, digital holography, and so on [11–24]. In many fields such as experimental mechanics and optics, the fringe projection profilometry (FPP) and the 3D digital image correlation (3D-DIC) methods are among the most established and widely

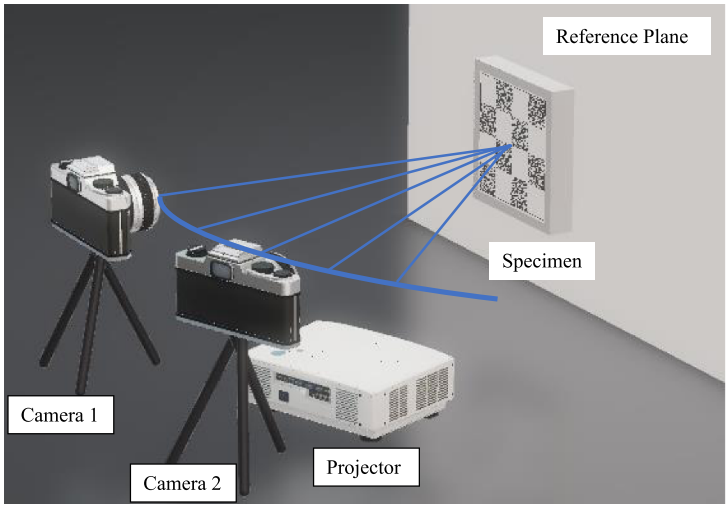

Figure 1. 3D schematic of the proposed stereo imaging.

used 3D imaging and shape measurement techniques owing to their robustness and accuracy [25–32]. The FPP technique, a kind of structured-light-based method, generally includes a projector, a camera, and a computer. The technique involves projecting active fringe patterns onto the target objects and capturing the distorted fringe patterns. The 3D shape information can then be extracted from the distorted fringe patterns. Unlike the FPP technique, the 3D-DIC technique is a stereo-vision-based method that heavily relies on detecting the stereo correspondence between two image sets captured by two cameras at different viewpoints, where the 3D coordinate information can be retrieved through using geometric triangulation upon the completion of camera calibration. It should be noted that the TOF method has recently become popular in certain applications including augmented reality, smartphones, autonomous vehicles, etc. Nevertheless, the TOF method faces the problem of relatively low resolution and low accuracy [33–36], and is thus not included in this work.

Over the years, numerous algorithms and schemes have been developed to enhance the performances of the FPP-based and DIC-based 3D imaging and shape measurements [37–46]. Many attempts have been made to improve the accuracy of the FPP-based systems such as building a mathematical model to reduce the measurement error [47–50], increasing the calibration accuracy with a liquid crystal display screen [51], and using customized fringes to enhance the sensitivity of phase detection [52]. Plenty of approaches have meanwhile been proposed to enhance the DIC-based systems such as utilizing a novel search scheme to improve the accuracy of the initial guess values [53] and using a multi-process parallel algorithm to increase the processing speed while maintaining the accuracy [54]. Recently, the integration of deep learning methods into stereo vision and fringe projection techniques [55–61] draw a surge of interest due to the advancements in automatic end-to-end learning networks as well as high-speed parallel computing, but their common shortcoming is the inferior accuracy. Despite these advances, an investigation into analyzing the relation of system geometry to measurement accuracy and comparing the accuracy of the two techniques under identical measurement conditions is lacking. Such an investigation helps provide a guideline on achieving the best possible measurement accuracy in practice, which is the motivation of this paper.

Figure 1 illustrates the arrangement of the projector and cameras used in the experiment, which allows simultaneously conducting both FPP and DIC measurements under the same geometry configurations. The study helps answer a frequently asked question: does the FPP technique or the 3D-DIC technique yield higher accuracy in the 3D imaging and shape measurement?

The following of the paper is organized as follow: section 2 describes the principles of the adopted FPP and 3D-DIC techniques as well as the indispensable camera calibration; section 3 presents experimental investigation into the measurement accuracy of the two techniques and a few experiments to demonstrate the capabilities of the techniques; and a summary with a brief discussion is included in the last section.

2. Principles of the techniques

2.1. Camera calibration

In the human eye system, the mind combines two separate images to build a 3D stereo picture by matching up similarities and adding in differences. This natural vision mechanism is commonly employed in the 3D

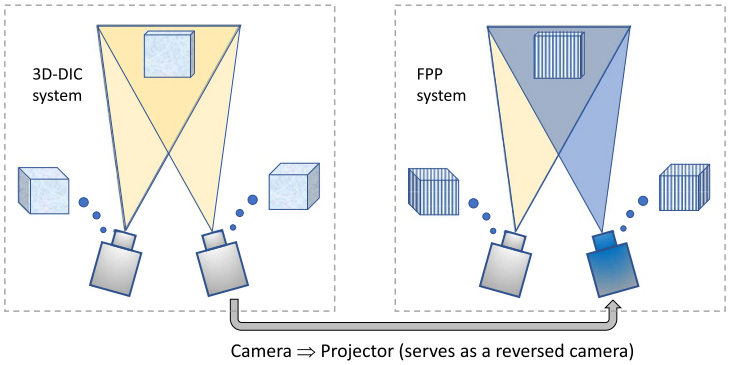

Figure 2. System similarity and difference of the FPP and 3D-DIC techniques.

machine vision field, and the 3D-DIC technique is one of such 3D imaging methods. By replacing one of the cameras with a projector, as illustrated in figure 2, the 3D-DIC imaging system becomes an FPP 3D imaging system. Because a projector is technically a reversed camera, the fundamental principles of the FPP and 3D-DIC techniques are similar: both are inherently based on binocular stereo imaging or triangulation imaging. Their primary difference lies in the way how image matching and determination of 3D coordinates are facilitated. Since both techniques rely on using cameras, camera calibration is described below.

The camera calibration describes the relation between the 3D world coordinates of a point and its corresponding location in the planar digital image. With a basic coordinate transformation, an arbitrary point (x_w, y_w, z_w) in the world coordinate system can be transformed into a camera coordinate system as (x_c, y_c, z_c) by using:

$$\begin{Bmatrix} x_c \\ y_c \\ z_c \end{Bmatrix} = \begin{bmatrix} R_{11} & R_{12} & R_{13} & T_1 \\ R_{21} & R_{22} & R_{23} & T_2 \\ R_{31} & R_{32} & R_{33} & T_3 \end{bmatrix} \begin{Bmatrix} x_w \\ y_w \\ z_w \\ 1 \end{Bmatrix}. \tag{1}$$

In the equation, R and T components, known as camera extrinsic parameters, indicate the rotation and translation parameters. Next, in the imaging plane of the camera, the pixel location (u, v) of the aforementioned point can be described with a pinhole model as:

$$\begin{Bmatrix} u \\ v \\ 1 \end{Bmatrix} = \frac{1}{z_c} \begin{bmatrix} \alpha & \gamma & u_0 \\ 0 & \beta & v_0 \\ 0 & 0 & 1 \end{bmatrix} \begin{Bmatrix} x_c \\ y_c \\ z_c \end{Bmatrix} = \begin{bmatrix} \alpha & \gamma & u_0 \\ 0 & \beta & v_0 \\ 0 & 0 & 1 \end{bmatrix} \begin{Bmatrix} x_{\mathrm{cn}} \\ y_{\mathrm{cn}} \\ 1 \end{Bmatrix}, \tag{2}$$

where $x_{\mathrm{cn}} = x_c/z_c$; $y_{\mathrm{cn}} = y_c/z_c$; α and β are the horizontal and vertical distances in pixel unit from the lens to the imaging plane, respectively; γ is a skew factor; and (u_0, v_0) is the coordinates of the principal point. The last five parameters are often termed the camera intrinsic parameters.

Considering the lens distortion in practice, the actual pixel location $(\widetilde{u}, \widetilde{v})$ of the point in the captured digital image can be modeled from equation (2) as:

$$\begin{Bmatrix} \widetilde{u} \\ \widetilde{v} \\ 1 \end{Bmatrix} = \begin{bmatrix} \alpha & \gamma & u_0 \\ 0 & \beta & v_0 \\ 0 & 0 & 1 \end{bmatrix} \begin{Bmatrix} \widetilde{x}_{\mathrm{cn}} \\ \widetilde{y}_{\mathrm{cn}} \\ 1 \end{Bmatrix}, \tag{3}$$

where

$$\begin{aligned} \widetilde{x}_{\mathrm{cn}} &= \left(1 + a_0 r^2 + a_1 r^4 + a_2 r^6 + a_3 r^8 + a_4 r^{10}\right) x_{\mathrm{cn}} \\ &\quad + \left(s_0 + s_2 r^2\right) r^2 + \left(p_0 + p_2 r^2\right) \left(r^2 + 2{x_{\mathrm{cn}}}^2\right) \\ \widetilde{y}_{\mathrm{cn}} &= \left(1 + a_0 r^2 + a_1 r^4 + a_2 r^6 + a_3 r^8 + a_4 r^{10}\right) y_{\mathrm{cn}} \\ &\quad + \left(s_1 + s_3 r^2\right) r^2 + \left(p_1 + p_3 r^2\right) \left(r^2 + 2{y_{\mathrm{cn}}}^2\right). \end{aligned} \tag{4}$$

In equation (4), $r^2 = {x_{\mathrm{cn}}}^2 + {y_{\mathrm{cn}}}^2$; $(a_0, \ldots, a_4)$, $(s_0, \ldots, s_3)$, and $(p_0, \ldots, p_3)$ represent radial, prism, and tangential distortion coefficients, respectively.

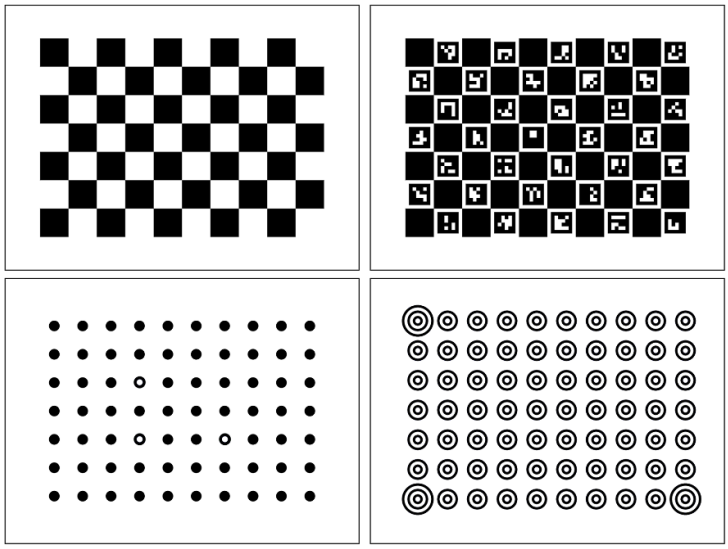

Figure 3. Example of different planar targets for camera calibration.

It is evident that equations (1)–(4) yield the relation between the 3D world coordinates of a point (x_w, y_w, z_w) and its pixel location $(\widetilde{u}, \widetilde{v})$ in the captured image. Through using a camera calibration target where the 3D world coordinates of the control points (such as the corner points of a checkerboard target) are known, the camera intrinsic and extrinsic parameters, as well as the lens distortion parameters, can be determined from a bundle-adjustment-based camera calibration process. Figure 3 show four commonly-used planar calibration targets. The relevant calibration algorithms can be found in [62–66].

A binocular imaging system contains two separate cameras. Thus, for a typical point (x_w, y_w, z_w) in the world coordinate system, equation (1) yields the following equations:

$$\begin{Bmatrix} x_{\mathrm{cn}} z_c \\ y_{\mathrm{cn}} z_c \\ z_c \end{Bmatrix} = \begin{bmatrix} R_{11} & R_{12} & R_{13} & T_1 \\ R_{21} & R_{22} & R_{23} & T_2 \\ R_{31} & R_{32} & R_{33} & T_3 \end{bmatrix} \begin{Bmatrix} x_w \\ y_w \\ z_w \\ 1 \end{Bmatrix}$$

$$\begin{Bmatrix} x'_{\mathrm{cn}} z'_c \\ y'_{\mathrm{cn}} z'_c \\ z'_c \end{Bmatrix} = \begin{bmatrix} R'_{11} & R'_{12} & R'_{13} & T'_1 \\ R'_{21} & R'_{22} & R'_{23} & T'_2 \\ R'_{31} & R'_{32} & R'_{33} & T'_3 \end{bmatrix} \begin{Bmatrix} x_w \\ y_w \\ z_w \\ 1 \end{Bmatrix}, \tag{5}$$

where the terms with a $'$ symbol are associated with the second camera. In equation (5), the extrinsic parameters R, T, R', and T' are acquired in advance from the calibration of the two cameras; x_{cn}, y_{cn}, x'_{cn}, and y'_{cn} can be obtained from the captured images using equations (3) and (4). Consequently, if the physical point corresponding to $(x_{\mathrm{cn}}, y_{\mathrm{cn}})$ in the first image is the same point corresponding to $(x'_{\mathrm{cn}}, y'_{\mathrm{cn}})$ in the second image, then there are totally six equations as shown in (5) and five unknowns: x_w, y_w, z_w, z_c, and z'_c. It is an overdetermined system, so the desired 3D world coordinates (x_w, y_w, z_w) can be solved. This explains why in theory a binocular imaging system can be employed for 3D imaging and shape measurements.

In practice, the FPP and 3D-DIC techniques adopt different approaches to facilitate the process of the 3D coordinates determination. The two techniques are elaborated as follows.

2.2. Fringe projection profilometry

The FPP setup is formed by replacing one of the two cameras in the binocular imaging system with a projector. A tremendous amount of work has been accomplished since the 1980s in the research and development of the FPP-based techniques. As technology evolves at an ever-increasing pace, accuracy has become the most important feature for the FPP technique in countless applications. Among the various approaches to implementing the FPP measurement, a considerably reliable scheme involves projecting a set of phase-shifted sinusoidal fringe patterns from a projector onto the objects, where the surface depth or height information is naturally encoded into the camera-captured fringe patterns. The technique reconstructs the 3D shapes through determining the height or depth map from the phase distributions of the

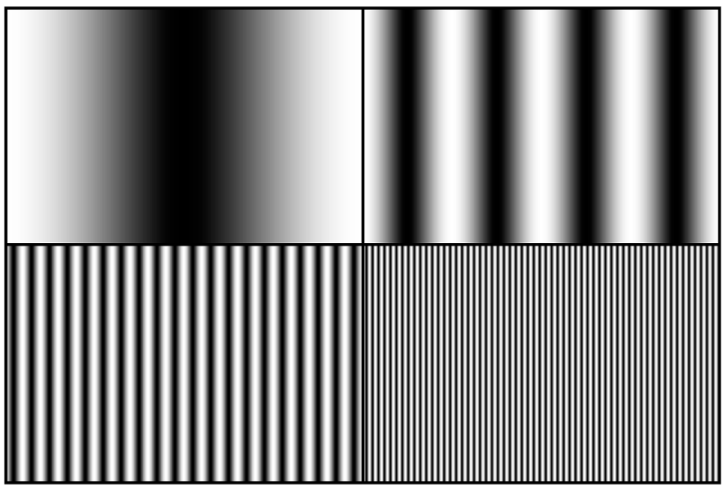

Figure 4. Fringe projection patterns with frequencies of 1, 4, 20, and 60.

captured fringes. In general, the original fringes are straight, evenly spaced, and vertically (or horizontally) oriented. They are numerically generated from using the following function [67, 68]:

$$I_j(u,v) = I_0\left[1+\cos(\phi+\delta_j)\right] = I_0\left[1+\cos(2\pi f\frac{u}{W}+\delta_j)\right], \tag{6}$$

where I is the pattern intensity at pixel coordinates (u, v); the subscript j denotes the jth phase-shifted image with $j = \{1, 2, \ldots, m\}$, and m is the number of the phase-shift steps (e.g. $m = 4$); I_0 is a constant coefficient indicating the intensity modulation; f is the number of fringes in the pattern image; W is the width of the generated image; δ is the phase-shift amount; and ϕ is the fringe phase. Figure 4 demonstrate four representative fringe patterns with various frequencies of 1, 4, 20, and 60, respectively.

The fringe phase at a pixel in the camera-captured images can be calculated by using a standard four-step phase-shifting algorithm as:

$$\phi^w(u,v) = \arctan\frac{I_4(u,v)-I_2(u,v)}{I_1(u,v)-I_3(u,v)}. \tag{7}$$

Because the equation uses an arctangent function, the obtained phase value is wrapped in the range of 0 to 2π (denoted with a superscript w), and it must be unwrapped to obtain the true phase. However, phase unwrapping is often a difficult task for cases involving complex shapes and geometric discontinuities. In order to cope with this issue, a scheme of using multi-frequency fringe patterns is employed. The corresponding unwrapped phase can be calculated from:

$$\phi_i(u,v) = \phi_i^w(u,v) + \mathrm{INT}\left(\frac{\phi_{i-1}\frac{f_i}{f_{i-1}}-\phi_i^w}{2\pi}\right)2\pi \tag{8}$$

where i indicates the ith fringe-frequency pattern with $i = \{2, 3, \ldots, n\}$, and n is the number of fringe frequencies; INT represents the function of rounding to the nearest integer; f_i is the number of fringes in the ith projection pattern, with $f_n > f_{n-1} > \ldots > f_1 = 1$; and $\phi_1 = \phi_1^w$ is satisfied for $f_1 = 1$. The ratio between two adjacent fringe frequencies $\frac{f_i}{f_{i-1}}$ is normally smaller or equal to 5 to reduce the noise effect and ensure the reliability of the algorithm. A practical example is $n = 4$ with $f_4 = 100$, $f_3 = 20$, $f_2 = 4$, and $f_1 = 1$.
The essential task of the FPP technique is to retrieve the depth or height map from the calculated phase distributions of the highest frequency fringes. The governing equation for a generalized setup where the system components can be arbitrarily positioned [69, 70] is:

$$z_w = \frac{f_c}{f_d}$$

$$
\begin{aligned}
f_c = {} & 1 + c_1\phi + (c_2 + c_3\phi)u + (c_4 + c_5\phi)v + (c_6 + c_7\phi)u^2 \\
& + (c_8 + c_9\phi)uv + (c_{10} + c_{11}\phi)v^2 + (c_{12} + c_{13}\phi)u^3 \\
& + (c_{14} + c_{15}\phi)u^2v + (c_{16} + c_{17}\phi)uv^2 + (c_{18} + c_{19}\phi)v^3 \\
& + (c_{20} + c_{21}\phi)u^4 + (c_{22} + c_{23}\phi)u^3v + (c_{24} + c_{25}\phi)u^2v^2 \\
& + (c_{26} + c_{27}\phi)uv^3 + (c_{28} + c_{29}\phi)v^4 \\
f_d = {} & d_0 + d_1\phi + (d_2 + d_3\phi)u + (d_4 + d_5\phi)v + (d_6 + d_7\phi)u^2 \\
& + (d_8 + d_9\phi)uv + (d_{10} + d_{11}\phi)v^2 + (d_{12} + d_{13}\phi)u^3 \\
& + (d_{14} + d_{15}\phi)u^2v + (d_{16} + d_{17}\phi)uv^2 + (d_{18} + d_{19}\phi)v^3 \\
& + (d_{20} + d_{21}\phi)u^4 + (d_{22} + d_{23}\phi)u^3v + (d_{24} + d_{25}\phi)u^2v^2 \\
& + (d_{26} + d_{27}\phi)uv^3 + (d_{28} + d_{29}\phi)v^4
\end{aligned} \tag{9}
$$

where z_w is the height or depth at the point corresponding to the pixel (u, v) in the captured images, and it is also the z-coordinate of the point in the reference or world coordinate system; ϕ is the unwrapped phase of the highest-frequency fringe pattern at the same pixel; and $c_1 - c_{29}$ and $d_0 - d_{29}$ are constant coefficients associated with geometrical and other system parameters. The 59 coefficients can be determined by a calibration process using a few gage objects that have many points with z_w precisely known. Recalling that the camera calibration previously described yields the 3D coordinates of the control points on the calibration board with ultrahigh accuracy, so they can serve as the gage points for determining the 59 coefficients. The cost function of the corresponding non-linear least-squares optimization [70, 71] is:

$$
S = \sum_{i=1}^{k}\sum_{j=1}^{l}\left(\frac{f_c}{f_d} - Z_{ij}\right)^2 \tag{10}
$$

where Z_{ij} is the z-coordinate or height/depth information of lth control point on the calibration board obtained at the kth calibration position. The 59 coefficients can be easily determined by using the Levenberg–Marquardt algorithm or a similar non-linear least-squares algorithm.

After the determination of z_w, the remaining two coordinates x_w and y_w of the same point can be calculated according to equations (1)–(4) as:

$$
\begin{aligned}
x_w &= \frac{q_2t_3 - q_3t_2}{q_2t_1 - q_1t_2} \\
y_w &= \frac{q_1t_3 - q_3t_1}{q_1t_2 - q_2t_1},
\end{aligned} \tag{11}
$$

where

$$
\begin{aligned}
q_1 &= x_{\mathrm{cn}}R_{31} - R_{11} \\
q_2 &= x_{\mathrm{cn}}R_{32} - R_{12} \\
q_3 &= z_w(R_{13} - x_{\mathrm{cn}}R_{33}) + (T_1 - x_{\mathrm{cn}}T_3) \\
t_1 &= y_{\mathrm{cn}}R_{31} - R_{21} \\
t_2 &= y_{\mathrm{cn}}R_{32} - R_{22} \\
t_3 &= z_w(R_{23} - y_{\mathrm{cn}}R_{33}) + (T_2 - y_{\mathrm{cn}}T_3).
\end{aligned} \tag{12}
$$

2.3. 3D digital image correlation

The 3D-DIC technique is a stereo vision method that performs 3D imaging and shape measurements using two images captured by two separate cameras, typically one on the left side and the other on the right side. Recalling in equation (5) that $(x_{\mathrm{cn}}, y_{\mathrm{cn}})$ and $(x'_{\mathrm{cn}}, y'_{\mathrm{cn}})$ must be associated with the same physical point, it is therefore required that the DIC algorithm fulfills matching the points in one image (the reference) to their corresponding points in another image (the target) with subpixel accuracies.

For an arbitrary pixel $(\widetilde{u}_0, \widetilde{v}_0)$ in the reference image to be matched, a square subset region of $(2M+1) \times (2M+1)$ pixels with its center located at $(\widetilde{u}_0, \widetilde{v}_0)$ is selected in the DIC analysis as the reference subset, where M is a positive integer. The corresponding subset in the target image (i.e. the target subset) should be a homography transformation of the reference subset because they are the same region captured by two cameras from separate positions and directions. It is noted that the usage of subsets not only makes matching pixels be feasible but also helps reduce the noise effect. Denoting the disparity between the centers

of the two matching subset patterns as (ξ, η), the transformation function for the entire reference and target subsets can be expressed as [30]:

$$\begin{aligned}\widetilde{u}_i' &= \widetilde{u}_i + \xi + \Delta_u(\xi_u + \xi_{uu}\Delta_u + \xi_{uv}\Delta_v) + \Delta_v(\xi_v + \xi_{vv}\Delta_v)\\ \widetilde{v}_j' &= \widetilde{v}_j + \eta + \Delta_u(\eta_u + \eta_{uu}\Delta_u + \eta_{uv}\Delta_v) + \Delta_v(\eta_v + \eta_{vv}\Delta_v)\end{aligned} \tag{13}$$

where i and j range from $-M$ to M, $\Delta_u = \widetilde{u}_i - \widetilde{u}_0$, $\Delta_v = \widetilde{v}_j - \widetilde{v}_0$, and ξ, ξ_u, ξ_v, ξ_{uu}, ξ_{vv}, ξ_{uv}, η, η_u, η_v, η_{uu}, η_{vv}, and η_{uv} are the transformation parameters. These parameters can be determined by minimizing the least-squares-based correlation coefficient defined as [72]:

$$C = \frac{1}{(2\,\mathrm{M}+1)^2}\sum_{i=-M}^{M}\sum_{j=-M}^{M}\left[af_{ij}^2 + bf_{ij} + c - g_{ij}\right]^2, \tag{14}$$

where a and b are scale factors, c is an offset of intensity, and $f_{ij} = f(\widetilde{u}_i, \widetilde{v}_j)$ and $g_{ij} = g(\widetilde{u}_i', \widetilde{v}_j')$ indicate the intensity values at a pixel in the reference subset and the potential matching pixel in the target subset, respectively. The 15 unknowns, including 12 shape-transformation parameters and 3 intensity parameters (a, b and c), can be solved by using an iterative algorithm such as the Gauss–Newton or Levenberg–Marquardt algorithms [73–75]. During the iteration process, an interpolation operation should be carried out to obtain the intensity values at subpixel locations in the target subset [76], i.e. $g(\widetilde{u}_i', \widetilde{v}_i')$. It is also noteworthy that the introduction of the non-linear scale factor a into the cost function is to compensate for the possible non-linear intensity variations between the captured images for accuracy-enhanced measurements.

To better present the iteration and the derivation of the iterative equation, equation (14) can be rewritten in another form as:

$$C(\boldsymbol{p}) = \sum_{i=-M}^{M}\sum_{j=-M}^{M}\left[\zeta_{ij}(\boldsymbol{p})\right]^2 \tag{15}$$

where $\boldsymbol{p} = \{\xi, \xi_u, \xi_v, \xi_{uu}, \xi_{vv}, \xi_{uv}, \eta, \eta_u, \eta_v, \eta_{uu}, \eta_{vv}, \eta_{uv}, a, b, c\}^{\mathsf{T}}$, and $\zeta_{ij}(\boldsymbol{p}) = af_{ij}^2 + bf_{ij} + c - g_{ij}$. The best estimate of the mapping parameters is established by minimizing $C(\boldsymbol{p})$. This can be iteratively carried out by applying the Gauss–Newton algorithm to equation (15), which yields the governing equation as:

$$\boldsymbol{p}_{n+1} = \boldsymbol{p}_n - \left[\sum_{i=-M}^{M}\sum_{j=-M}^{M}\left(\boldsymbol{J}_{ij}\boldsymbol{J}_{ij}^T\right)\right]^{-1}\sum_{i=-M}^{M}\sum_{j=-M}^{M}\left[\zeta_{ij}(\boldsymbol{p})\boldsymbol{J}_{ij}\right] \tag{16}$$

where $n = 0, 1, 2, \ldots$ indicates the iteration step, and $\boldsymbol{J}_{ij}$ is the Jacobian vector defined as [77]:

$$\begin{aligned}\boldsymbol{J}_{ij} = \frac{\partial\zeta_{ij}(\boldsymbol{p})}{\partial\boldsymbol{p}} = -\{&g_{u_i'}, g_{u_i'}\Delta_u, g_{u_i'}\Delta_v, g_{u_i'}\Delta_u^2, g_{u_i'}\Delta_v^2,\\ &g_{u_i'}\Delta_u\Delta_v, g_{v_j'}, g_{v_j'}\Delta_u, g_{v_j'}\Delta_v, g_{v_j'}\Delta_u^2, g_{v_j'}\Delta_v^2, g_{v_j'}\Delta_u\Delta_v, -f_{ij}^2, -f_{ij}, -1\}^{\mathsf{T}}\end{aligned} \tag{17}$$

In equation (17), $g_{u_i'} = \frac{\partial g(\widetilde{u}_i', \widetilde{v}_j')}{\partial \widetilde{u}_i'}$ and $g_{v_j'} = \frac{\partial g(\widetilde{u}_i', \widetilde{v}_j')}{\partial \widetilde{v}_j'}$ are the intensity gradients of the target subset at location $(\widetilde{u}_i', \widetilde{v}_j')$ in the x- and y-directions, respectively. In the iteration, the convergence tolerance can be set to 1×10^{-5} for each element of $\boldsymbol{p}$.

The above iterative algorithm is capable of performing the image matching process with high accuracy at a very fast speed upon a reasonably good initial guess for the unknown transformation parameters which are mainly the low-order terms ξ, η, ξ_u, ξ_v, η_u, η_v in equation (13). Such an initial guess can be carried out by using a manual way of selecting three pairs of matching points in the reference and target images, or using an automatic full-field scanning process in the case of small shape change of the target subset with respect to the reference subset. A feature-based matching scheme may be employed to conduct the initial guess [78, 79] if the previous two schemes are not applicable.

Upon the completion of image matching, a pixel $(\widetilde{u}, \widetilde{v})$ in the region of interest in one image is now linked to a corresponding pixel $(\widetilde{u}', \widetilde{v}')$ in another image. From equations (3) and (4), $(x_{\mathrm{cn}}, y_{\mathrm{cn}})$ and $(x_{\mathrm{cn}}', y_{\mathrm{cn}}')$ can then be determined. Subsequently, by eliminating z_c and z_c', equation (5) yields

$$\begin{bmatrix} x_{\mathrm{cn}}R_{31} - R_{11} & x_{\mathrm{cn}}R_{32} - R_{12} & x_{\mathrm{cn}}R_{33} - R_{13}\\ y_{\mathrm{cn}}R_{31} - R_{21} & y_{\mathrm{cn}}R_{32} - R_{22} & y_{\mathrm{cn}}R_{33} - R_{23}\\ x_{\mathrm{cn}}'R_{31}' - R_{11}' & x_{\mathrm{cn}}'R_{32}' - R_{12}' & x_{\mathrm{cn}}'R_{33}' - R_{13}'\\ y_{\mathrm{cn}}'R_{31}' - R_{21}' & y_{\mathrm{cn}}'R_{32}' - R_{22}' & y_{\mathrm{cn}}'R_{33}' - R_{23}' \end{bmatrix}\begin{Bmatrix} x_w\\ y_w\\ z_w \end{Bmatrix} = \begin{Bmatrix} T_1 - x_{\mathrm{cn}}T_3\\ T_2 - y_{\mathrm{cn}}T_3\\ T_1' - x_{\mathrm{cn}}'T_3'\\ T_2' - y_{\mathrm{cn}}'T_3' \end{Bmatrix} \tag{18}$$

Equation (18) is an overdetermined equation system, and the desired (x_w, y_w, z_w) can be acquired from its linear least-squares solutions. That is, expressing the equation as $\boldsymbol{Ax} = \boldsymbol{B}$, and the solution is calculated from $\boldsymbol{x} = (\boldsymbol{A}^{\mathsf{T}}\boldsymbol{A})^{-1}\boldsymbol{A}^{\mathsf{T}}\boldsymbol{B}$.

3. Experiments

The FPP and 3D-DIC experiments have been implemented to investigate the variations of measurement accuracy induced by the geometric changes of hardware positions. The experiment system is composed of two EPIX SV9T001C cameras with a resolution of 2048 × 1536 pixels, an EPSON Powerlite 98 projector, and a desktop computer with an Intel Core i7-980 processor and 8GB RAM. The experiments use two planar calibration boards with 10 × 7 concentric-circle patterns on each, where the pattern spacings are 25.4 and 12.7 mm, respectively. The image capturing and analysis software is written in the C++ language, and the cameras and projector are synchronized by the software. The captured images are saved in the 8-bit bitmap format, which is uncompressed and lossless.

In order to achieve 3D shape measurements with high accuracy, a few measures have been taken for the experiments to isolate the noise sources. These measures include running the experiments in the basement lab, setting up the systems in an enclosure on an isolation optical table, and starting the experiment after thermal equilibrium is reached.

3.1. System geometry

The experiments adopt a typical distance of about 1 m from the cameras and projector to the target. Longer or shorter distances can be used, but they do not affect the goal of the accuracy comparison. The angle between the camera and the projector/camera positions in the experiment system plays a key role in affecting the measurement accuracy. In triangulation theory, the height or depth distinction can be more accurately detected if the baseline (i.e. the distance between the two cameras) increases. A longer baseline indicates a larger viewing angle between the cameras in the 3D-DIC technique or between the camera and the projector in the FPP technique. A larger angle leads to larger disparities of points in the images (here the projector is technically treated as a reversed camera for the FPP measurement), which theoretically helps enhance the measurement sensitivity and consequently accuracy. In practice, however, an increased angle causes larger affine transformation between the images, which may bring down the measurement accuracy. In addition, it often results in less overlapping regions to reconstruct the desired 3D shapes, and a large angle should be particularly avoided in the presence of excessive occlusions and shadows. On the other hand, a decrease in the angle may bring more difficulty in distinguishing the differences between images, which can further diminish the measurement accuracy.

In the experiments, the measurement accuracy of both techniques is investigated with different camera-camera or camera-projector angles ranging from 15° to 45° with an increment of 10°. Angles beyond this range are not considered because they are impractical in accurate real-world applications. In the system hardware setup, the two cameras are positioned symmetrically with respect to the reference plane (or the x–y plane of the world coordinate system), whereas the projector is located right below one of the cameras and oriented in the same direction, as previously illustrated in figure 1.

The access to an appropriate gage object whose height or depth is precisely known with sub-micron or nano-scale accuracy is unavailable in this work. Instead, the specimen target is a cuboid with its front surface covered by a special pattern as shown in figure 5, where the white and speckle regions are for the simultaneous FPP and 3D-DIC measurements, respectively. Under the cuboid is a translation stage, which is driven by a differential adjuster and piezoelectric actuator with a translation range of 0–25 μm at nanoscale accuracy. In addition, the front surface of the specimen target is positioned parallel with the reference plane and perpendicular to the motion direction of the translation stage. The adjustment and alignment operations are aided by using laser light and reflection mirrors. The inevitable small misalignment in practice is negligible since the induced error is relatively tiny. For instance, a 2° misalignment in the motion direction would result in an error of 0.006 μm for a movement of 10 μm. Furthermore, the relative and averaged position of the specimen surface is chosen as the physical quantity for accuracy assessment, and no additional noise-reduction process is applied to the techniques. It must be clarified that the 3D shape measurement accuracy is determined by the minimum depth change that can be detected, therefore a flat surface driven by an ultrahigh-resolution translation stage is employed.

The primary procedure of the experiments is as follows:

(a) Capture images for the system calibration. The FPP technique requires capturing 10–20 sets of the calibration board images at different positions with the left camera (for simplicity, the FPP measurement is assumed to use the left camera hereafter). At each position, multi-frequency phase-shifted fringes are

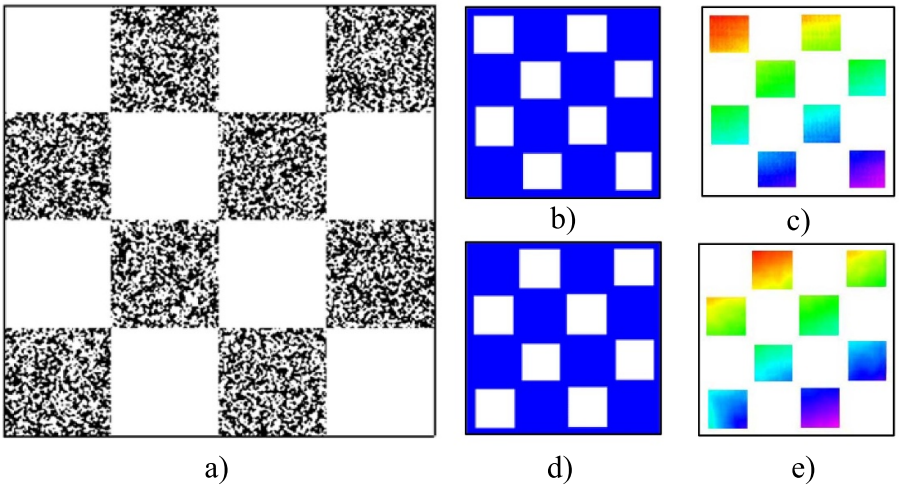

Figure 5. Speckle checkerboard patterns on the specimen surface and the illustration of masks and z-coordinate maps. The z-coordinate map is not uniform due to a small misalignment between the specimen surface and the x–y reference plane of the world coordinates.

Table 1. FPP-measured displacements with different camera-projector angles.

	Nominal positions				
	5	10	15	20	25
Angles	Measured errors				
15°	−0.465	−0.429	−0.565	−0.254	−0.460
25°	0.427	0.360	0.410	0.520	0.453
35°	0.572	0.512	0.646	0.568	0.583
45°	0.630	0.574	0.699	0.605	0.594

unit: μm

Table 2. DIC-measured displacements with different camera-camera angles.

	Positions				
	5	10	15	20	25
Angles	Measured errors				
15°	−0.360	−0.412	-0.488	0.322	−0.281
25°	0.351	0.410	0.459	0.560	0.572
35°	0.589	0.674	0.637	0.573	0.617
45°	0.642	0.702	0.681	0.658	0.655

unit: μm

projected on the board surface for the FPP technique. As mentioned previously, using four phase-shifted images for each frequency and four frequencies for each phase-unwrapping process implies a total of 16 images for each accurate FPP measurement. The 3D-DIC technique requires capturing only one image at each position with each of the cameras.

(b) Calibrate the two cameras, and then calibrate the 59 FPP coefficients. After this step, the calibration task is completed.

(c) Run the experiments by capturing a set of multi-frequency phase-shifted fringe images with the left camera for the FPP measurement and capturing a pair of images with both cameras for the DIC measurement. Then perform processing and analysis to acquire the 3D coordinate results for each technique. The measurements are carried out a few times with the specimen target translating with designated displacements.

(d) Change the camera-camera and camera-projector angle, and repeat the measurements.

(e) The above experiments are conducted five times to use the average results for accuracy assessment.

Tables 1 and 2 show the measurement errors of the out-of-reference-plane positions of the specimen target under four angle configurations. Because the initial position is not perfectly located on the x–y plane

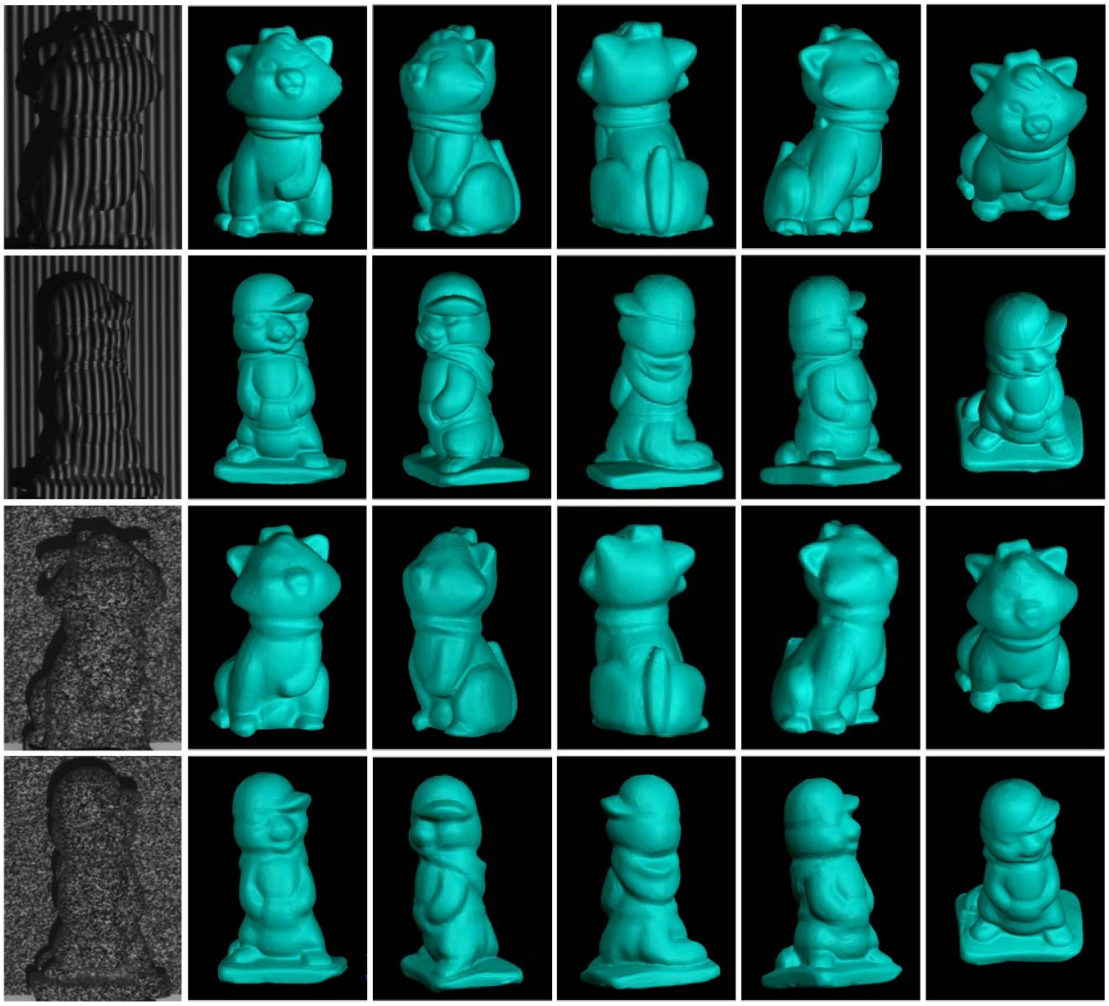

Figure 6. 360° 3D reconstruction results from the FPP and DIC techniques.

of the world coordinate system, the positions are calculated by subtracting the initial position from each new position after translating the target. It can be seen from the tables that the 25° configuration yields the best results. The results also reveal that the largest error of 0.699 μm occurs at 45° angle in the case of 15 μm displacement for the FPP measurements, and the largest error of 0.702 μm occurs at 45° angle in the case of 10 μm displacement for the 3D-DIC measurements. It is noteworthy that the largest errors seem to occur at a random distance because of system uncertainties, but the root cause is unclear.

The relative accuracy is defined as the ratio of out-of-plane measurement error to the in-plane width dimension. With the field of view being 415.0 mm wide in the experiments, the relative accuracy can be calculated as 0.000699 mm/415.0 mm $\approx$ 1/595 000 for the FPP technique and 0.000702 mm/415.0 mm $\approx$ 1/590 000 for the 3D-DIC technique. Overall, the measurement accuracy of both techniques is close to 1/600 000, indicating an ultrahigh accuracy. In the following experiments, the angle of 25° is adopted.

3.2. 360-degree 3D image reconstruction

To demonstrate the measurement accuracy of the FPP and 3D-DIC techniques, the 2-in-1 experiment system has been utilized to reconstruct 360° 3D images of some objects. The logic of this experiment is, without high measurement accuracy, building accurate 360° 3D images from multiple views would be difficult because of error accumulation.

In the experiment, the projector is utilized to project speckle patterns on the objects of interest owing to their lack of required surface texture. The measurement system is first positioned to obtain the 3D image of an object from a fixed view, and the measurement is then repeated by rotating the object to cover the entire surface. Totally ten different 3D images are acquired and combined to form a complete 360° 3D image. Figure 6 shows the 3D images reconstructed from the two techniques where the first image in each row is cropped from one of the original images captured for the corresponding technique and the remaining images are selected views of the reconstructed 360° 3D image. In the figure, the first two rows demonstrate

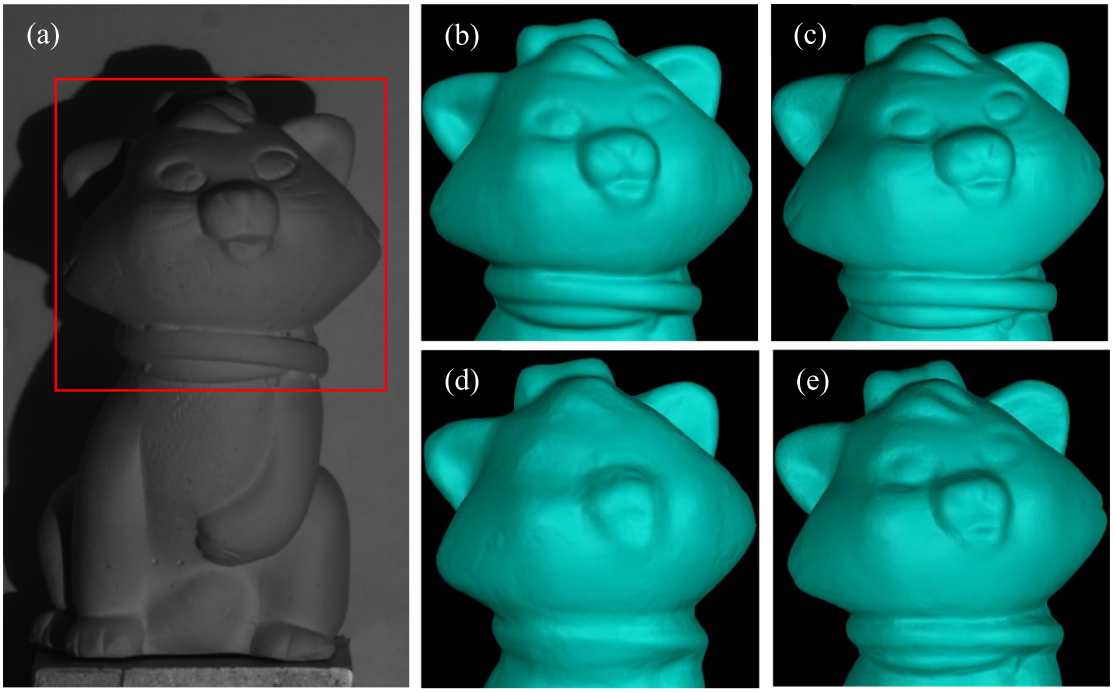

Figure 7. 3D reconstruction results from the FPP and 3D-DIC techniques from two different imaging resolutions. (a) is a grayscale image of the object with a region of interest (ROI) selected. (b)–(c) represent the 3D results from the FPP measurements at initial and higher spatial resolutions, respectively. (d)–(e) demonstrate the 3D results from the 3D-DIC measurements at initial and higher resolutions, respectively.

representative results acquired by the FPP technique, and the following two rows show representative results obtained by the 3D-DIC technique. Because the true dimensions of those objects are unknown, visual assessment is employed here.

By successfully generating the 360° 3D images, the experiments help verify the capabilities of the FPP and 3D-DIC techniques in terms of measurement accuracy.

3.3. System resolution

Results presented in figure 6 show different resolutions for the FPP and 3D-DIC techniques. Such an issue of resolution is not able to be revealed from the previous accuracy test since the specimen is planar. Therefore, an experiment on system resolution is conducted.

In this experiment, the field of view is reduced to about half of the previous experiments and a smaller calibration board with a grid distance of 12.7 mm is adopted. In the meantime, the camera-camera and camera-projector angles as well as the test objects remain unchanged. Figure 7 displays the comparison of the acquired 3D reconstruction results with the ones obtained in the previous experiments. It is evident from a visual comparison that higher resolution can substantially improve the performance of both techniques, especially the 3D-DIC one. The reason is that the higher resolution of the cameras gives more detail for the local regions, and the resolution of the 3D results is accordingly improved. Because the DIC algorithm highly depends on local information for disparity detection, the improvement is visually more distinct.

3.4. Multiple separate objects

The ever-broadening applications have driven the 3D imaging and shape measurement techniques to possess the capability of handling geometric discontinuity and acquiring 3D images of multiple separated objects in the field of view simultaneously. For this reason, the fourth experiment has been implemented to demonstrate such a capability. Representative results presented in figure 8 validate that both techniques can cope well with geometric discontinuities. Again, it is shown that the FPP technique outperforms the DIC technique in terms of local detail due to the pixel-by-pixel processing versus subset-based analysis.

4. Conclusion

This paper has presented an experimental investigation into the accuracy comparison of two popular techniques for the 3D imaging and 3D shape measurements: the FPP and 3D-DIC techniques. It is revealed that the fundamental principles of the two techniques are both based on binocular stereo vision, or more

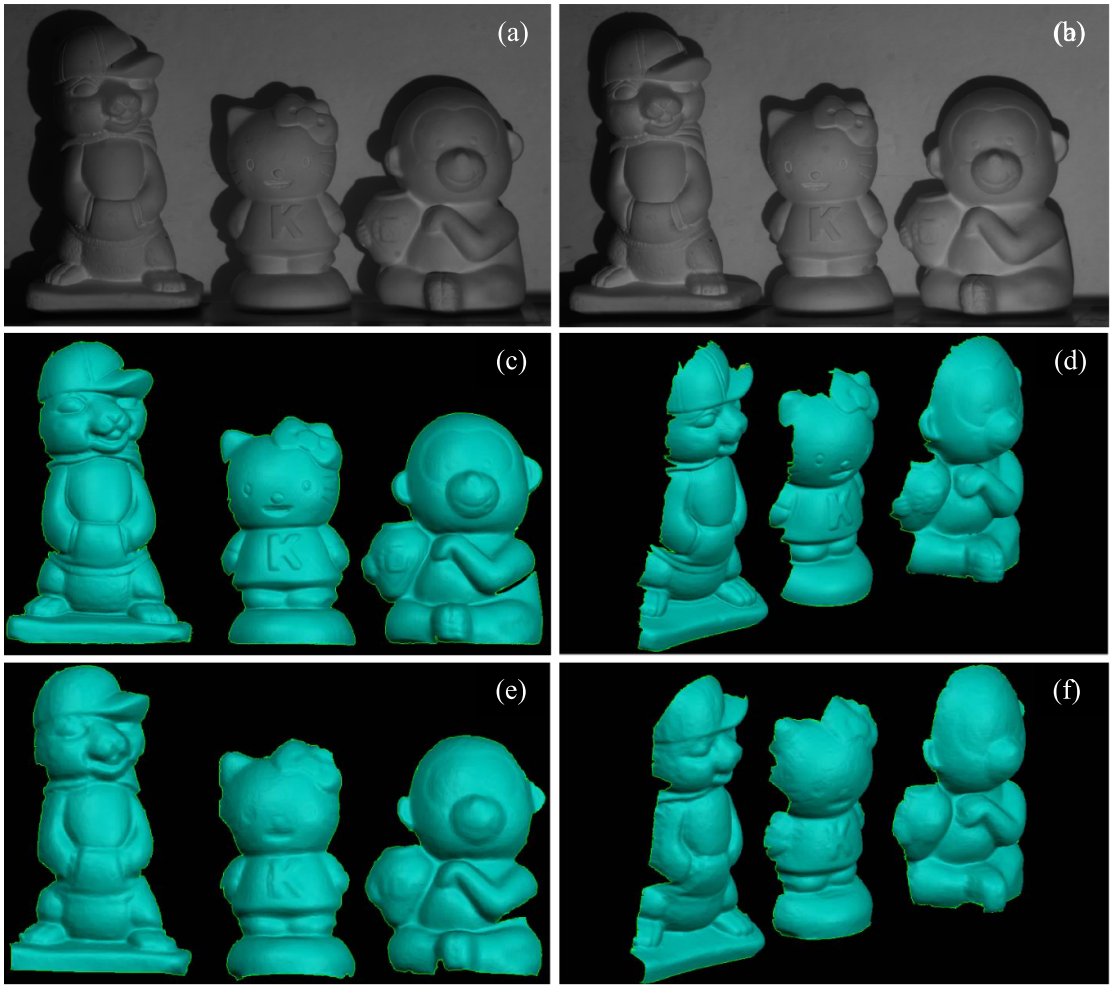

Figure 8. 3D image reconstruction of multiple separated objects. (a)–(b) are captured grayscale images by two cameras; (c)–(d) are two different views of the 3D results obtained from the FPP measurement; (e)–(f) are the results from the 3D-DIC measurement.

rigorously, triangulation imaging. Their main difference is that the FPP technique employs fringe patterns to facilitate the image correspondence detection, while the DIC technique uses speckle or texture patterns to carry out the image matching task. By using a measurement system composed of both the FPP and the 3D-DIC techniques, an evaluation on how the geometric angles between key hardware components affect the 3D measurement accuracy is accomplished for both methods. It turns out that the depth and height measurements of both techniques can reach sub-micron accuracy, and the relative accuracy of the 3D shape or position measurements can reach 1/600 000 for both techniques. The results indicate that the accuracy of depth measurement can be close to that of the classical optical interferometry techniques such as Twyman–Green interferometry and Fizeau interferometry [80].

It is important to point out that the acquired ultrahigh accuracy is based on detecting the average location changes of a flat plane, so the noise influence is quite low in the assessment. The investigation considers only the rigid-body translations because their ground-truth values can be assured. Moreover, since the accuracy of the 3D shape measurement is fundamentally the ability to detect the smallest depth or height change, it is technically reasonable and sufficient to study solely the translations.

For both techniques, the accuracy is substantially higher than the resolution. Specifically, the accuracy can reach sub-micron level and the typical resolution is at the scale of tens of microns. Consequently, the resolution will be dominant in actual applications where local details are often of interest. Because the FPP algorithm is based on pixel-by-pixel processing and the DIC algorithm is based on subset-matching analysis, the FPP measurement outperforms the 3D-DIC measurement in terms of resolution. Nevertheless, the resolution of cameras has been improving at a pace much faster than that of projectors; therefore, the resolution is not a practical problem in the applications of the 3D-DIC technique. The major problem with the 3D-DIC technique remains the analysis speed, though speed evaluation is another topic beyond the scope of this paper.

At present, the leading commercial structured-light-based 3D scanners can provide accuracy up to a couple of microns. In recent years, there has been a high demand for the 3D imaging and shape measurement techniques to provide ultrahigh accuracy. The system presented in this paper has demonstrated the capability of satisfying this ascending demand.

ORCID iDs

Hieu Nguyen https://orcid.org/0000-0002-5154-0125
Jiali Liang https://orcid.org/0000-0002-9821-7325
Zhaoyang Wang https://orcid.org/0000-0002-6384-3107

References

[1] Remondino F and El-Hakim S 2006 Image-based 3D modelling: a review *The Photogrammetric Rec.* **21** 269–91
[2] Sansoni G, Trebeschi M and Docchio F 2009 State-of-the-art and applications of 3D imaging sensors in industry, cultural heritage, medicine and criminal investigation *Sensors* **9** 568–601
[3] Blais F 2004 Review of 20 years of range sensor development *J. Electron. Imaging.* **13** 231–43
[4] Chen F, Brown G M and Song M 2000 Overview of three-dimensional shape measurement using optical methods *Opt. Eng.* **39** 10–22
[5] Su X and Zhang Q 2010 Dynamic 3-d shape measurement method: a review *Opt. Lasers Eng.* **48** 191–204
[6] Geng J 2011 Structured-light 3D surface imaging: a tutorial *Adv. Opt. Photonics.* **3** 128–60
[7] Wu R, Wu H, Arola D and Zhang D 2016 Real-time three-dimensional digital image correlation for biomedical applications *J. Biomed. Opt.* **21** 107003
[8] Zhang S 2018 High-speed 3D shape measurement with structured light methods: a review *Opt. Lasers Eng.* **106** 119–31
[9] Ma Z and Liu S 2018 A review of 3d reconstruction techniques in civil engineering and their applications *Adv. Eng. Inf.* **38** 163–74
[10] Nguyen H, Kieu H, Wang Z and Le H 2018 Three-dimensional facial digitization using advanced digital image correlation *Appl. Opt.* **57** 2188–96
[11] Oliveira F and Tavares J 2014 Medical image registration: a review *Comput. Methods. Biomech. Biomed. Eng.* **17** 73–93
[12] Cui Y, Schuon S, Chan D, Thrun S and Theobalt C 2010 3d shape scanning with a time-of-flight camera *Conf. on Computer Vision and Pattern Recognition (CVPR)* (IEEE) pp 1173–80
[13] El-Omari S and Moselhi O 2008 Integrating 3D laser scanning and photogrammetry for progress measurement of construction work *Autom. Constr.* **18** 1–9
[14] Gorthi S S and Rastogi P 2010 Fringe projection techniques: whither we are? *Opt. Lasers Eng.* **48** 133–40
[15] Espinosa J, Perez J, Ferrer B and Mas D 2015 Method for targetless tracking subpixel in-plane movements *Appl. Opt.* **54** 7760–5
[16] Nguyen H, Wang Z, Jones P and Zhao B 2017 3d shape, deformation and vibration measurements using infrared kinect sensors and digital image correlation *Appl. Opt.* **56** 9030–7
[17] Hamzah R A and Ibrahim H 2016 Literature survey on stereo vision disparity map algorithms *J. Sensors* 8742920
[18] Brodoline A, Rawat N, Alexandre D, Cubedo N and Gross M 2019 4d compressive sensing holographic microscopy imaging of small moving objects *Opt. Lett.* **44** 2827–30
[19] Jeon S, Lee J-Y, Cho J, Jang S-H, Kim Y-J and Park N-C 2018 Wavelength-multiplexed digital holography for quantitative phase measurement using quantum dot film *Opt. Express* **26** 27305–13
[20] Kumar M, Quan X, Awatsuji Y, Cheng C, Hasebe M, Tamada Y and Matoba O 2020 Common-path multimodal three-dimensional fluorescence and phase imaging system *J. Biomed. Opt.* **25** 1–15
[21] Tahara T and Endo Y 2019 Multiwavelength-selective phase-shifting digital holography without mechanical scanning *Appl. Opt.* **58** G218–25
[22] Tahara T, Ishii A, Ito T, Ichihashi Y and Ryutaro O 2020 Single-shot wavelength-multiplexed digital holography for 3D fluorescent microscopy and other imaging modalities *Appl. Phys. Lett.* **117** 031102
[23] Kumar M, Birhman A S, Kannan S and Shakher C 2018 Measurement of initial displacement of canine and molar in human maxilla under different canine retraction methods using digital holographic interferometry *Opt. Eng.* **57** 1–12
[24] Tavera Ruiz C G, De La Torre-Ibarra M H, Flores-Moreno J M, Frausto-Reyes C and Santoyo F M 2018 Cortical bone quality affectations and their strength impact analysis using holographic interferometry *Biomed. Opt. Express* **9** 4818–33
[25] Zuo C, Feng S, Huang L, Tao T, Yin W and Chen Q 2018 Phase shifting algorithms for fringe projection profilometry: a review *Opt. Lasers Eng.* **109** 23–59
[26] Quan C, Chen W and Tay C J 2010 Phase-retrieval techniques in fringe-projection profilometry *Opt. Lasers Eng.* **48** 235–43
[27] Zhang S 2018 Absolute phase retrieval methods for digital fringe projection profilometry: a review *Opt. Lasers Eng.* **107** 28–37
[28] Nguyen H, Nguyen D, Wang Z, Kieu H and Le M 2015 Real-time, high-accuracy 3d imaging and shape measurement *Appl. Opt.* **54** A9–17
[29] Wang Z, Kieu H, Nguyen H and Le M 2015 Digital image correlation in experimental mechanics and image registration in computer vision: similarities, differences and complements *Opt. Lasers Eng.* **65** 18–27
[30] Pan B, Qian K, Xie H and Asundi A 2009 Two-dimensional digital image correlation for in-plane displacement and strain measurement: a review *Meas. Sci. Tech.* **20** 062001
[31] Blaber J, Adair B and Antoniou A 2015 Ncorr: Open-source 2d digital image correlation matlab software *Exp. Mech.* **66** 1105–22
[32] Hild F and Roux S 2012 Comparison of local and global approaches to digital image correlation *Exp. Mech.* **52** 1503–19
[33] Yan X, Ao L and Yang X 2018 Three-dimensional pose measurement method of non-cooperative rectangular target based on time-of-flight camera *Appl Res Comp/Jisuanji Yingyong Yanjiu* **35** 2856–60
[34] Hubner P, Clintworth P, K, Liu Q, Weinmann M and Wursthorn S 2020 Evaluation of Hololens tracking and depth sensing for indoor mapping applications *Sensors* **20** 1021
[35] Overton G 2018 3d tof camera technology improves facial recognition accuracy and security *Laser Focus World* **54** 21–2
[36] Zalud L, Kotova M, Kocmanova P, Dobsak P and Kolarova J 2016 Breath analysis using a time-of-flight camera and pressure belts *Artif. Organs.* **40** 619–26

[37] Pan B, Xie H, Xu B and Dai F 2006 Performance of sub-pixel registration algorithms in digital image correlation *Meas. Sci. Tech.* **17** 1615
[38] Shao X, Dai X, Chen Z and He X 2016 Real-time 3D digital image correlation method and its application in human pulse monitoring *Appl. Opt.* **55** 696–704
[39] Gao Y, Cheng T, Su Y, Xu X, Zhang Y and Zhang Q 2015 High-efficiency and high-accuracy digital image correlation for three-dimensional measurement *Opt. Lasers Eng.* **65** 73–80
[40] Wu R, Kong C, Li K and Zhang D 2016 Real-time digital image correlation for dynamic strain measurement *Exp. Mech.* **56** 833–43
[41] Xu J, Xi N, Zhang C, Shi Q and Gregory J 2011 Real-time 3D shape inspection system of automotive parts based on structured light pattern *Opt. Laser Tech.* **43** 1–8
[42] Zuo C, Chen Q, Gu G, Feng S, Feng F, Li R and Shen Q 2013 High-speed three-dimensional shape measurement for dynamic scenes using bi-frequency tripolar pulse-width-modulation fringe projection *Opt. Lasers Eng.* **51** 953–60
[43] Felipe-Sese L, Molina-Viedma A J, Lopez-Alba E and Diaz F A 2019 FP+DIC for low-cost 3D full-field experimental modal analysis in industrial components *Mech. Syst. Sig. Proc.* **128** 329–39
[44] Molina-Viedma A J, Felipe-Sese L, Lopez-Alba E and Diaz F A 2020 Comparative of conventional and alternative digital image correlation techniques for 3D modal characterisation *Measurement* **151** 107101
[45] Cheng X, Liu X, Li Z, Zhong K, Han L and He W 2019 High-accuracy globally consistent surface reconstruction using fringe projection profilometry *Sensors* **19** 668
[46] Nguyen H, Dunne N, Li H, Wang Y and Wang Z 2019 Real-time 3D shape measurement using 3 LCD projection and deep machine learning *Appl. Opt.* **58** 7100–9
[47] Yang T, Zhang G, Li H, Zhang Z and Zhou X 2019 Theoretical proof of parameter optimization for sinusoidal fringe projection profilometry *Opt. Lasers Eng.* **123** 37–44
[48] Lv S, Jiang M, Su C, Zhang L, Sui Q and Jia L 2019 Flexible calibration method of an FPP system based on a geometrical model and NLSM with fewer parameters *Appl. Opt.* **58** A7–12
[49] Li K, Bu J and Zhang Z 2016 Lens distortion elimination for improving measurement accuracy of fringe projection profilometry *Opt. Lasers Eng.* **85** 53–64
[50] Huang Z, Xi J, Yu Y, Guo Q and Song L 2014 Improved geometrical model of fringe projection profilometry *Opt. Express* **22** 32220–32
[51] Chen C, Yu J, Gao N and Zhang Z 2020 High accuracy 3d calibration method of phase calculation-based fringe projection system by using LCD screen considering refraction error *Opt. Lasers Eng.* **126** 105870
[52] Yu J, Gao N, Zhang Z and Meng Z 2020 High sensitivity fringe projection profilometry combining optimal fringe frequency and optimal fringe direction *Opt. Lasers Eng.* **129** 106068
[53] Lin Z, Cai T and Wang Y 2019 An accelerated and accurate process for the initial guess calculation in digital image correlation algorithm *Insight: Non-Destr Testing Cond Monit* **61** 729–37
[54] Zhang J, Lu H and Baroud G 2018 An accelerated and accurate process for the initial guess calculation in digital image correlation algorithm *AIMS Mater. Sci.* **5** 1223–41
[55] Li P, Chen X and Shen S 2019 Stereo R-CNN based 3D object detection for autonomous driving *Conf. on Computer Vision and Pattern Recognition (CVPR)* (IEEE) pp 7644–52
[56] Luo W, Schwing A G and Urtasun R 2016 Efficient deep learning for stereo matching *Conf. on Computer Vision and Pattern Recognition (CVPR)* (IEEE) pp 5695–703
[57] Chang J and Chen Y 2018 Pyramid stereo matching network *Conf. on Computer Vision and Pattern Recognition (CVPR)* (IEEE) pp 5410–18
[58] Nguyen H, Wang Y and Wang Z 2020 Single-shot 3D shape reconstruction using structured light and deep convolutional neural networks *Sensors* **20** 3718
[59] Feng S, chen Q, Gu G, Tao T, Zhang L, Hu Y, Yin W and Zuo C 2019 Fringe pattern analysis using deep learning *Adv. Photonics* **1** 025001
[60] Feng S, Zuo C, Win W, Gu G and Chen Q 2019 Micro deep learning profilometry for high-speed 3D surface imaging *Opt. Lasers Eng.* **121** 416–27
[61] Jeught S and Dirckx J 2019 Deep neural networks for single shot structured light profilometry *Opt. Express* **27** 17091–101
[62] Vo M, Wang Z, Luu L and Ma J 2011 Advanced geometric camera calibration for machine vision *Opt. Eng.* **50** 110503
[63] Douxchampx D and Chihara K 2009 High-accuracy and robust localization of large control markers for geometric camera calibration *IEEE Trans. Patt. Anal. Mach. Intell.* **31** 376–83
[64] Furukawa Y and Ponce J 2009 Accurate camera calibration from multi-view stereo and bundle adjustment *Int. J. Comp. Vis.* **84** 257–68
[65] Monero D and Taubin G 2012 Simple, accurate and robust projector-camera calibration *IEEE Int. Conf. on 3D Imaging, Modeling, Processing, Visualization & Transmission* pp 464–71
[66] Zhang Z 2000 A flexible new technique for camera calibration *IEEE Trans. Patt. Anal. Mach. Intell.* **22** 1330–4
[67] Le H, Nguyen H, Wang Z, Opfermann J, Leonard S, Krieger A and Kang J 2018 Demonstration of a laparoscopic structured-illumination three-dimensional imaging system for guiding reconstructive bowel anastomosis *J. Biomed. Opt.* **23** 056009
[68] Wang Z, Nguyen D and Barnes J 2010 Some practical considerations in fringe projection profilometry *Opt. Lasers Eng.* **48** 218–25
[69] Du H and Wang Z 2007 Three-dimensional shape measurement with an arbitrarily arranged fringe projection profilometry system *Opt. Lett.* **32** 2438–40
[70] Vo M, Wang Z, Pan B and Pan T 2012 Hyper-accurate flexible calibration technique for fringe-projection-based three-dimensional imaging *Opt. Express* **20** 16926–41
[71] Vo M, Wang Z, Hoang T and Nguyen D 2010 Flexible calibration technique for fringe-projection-based three-dimensional imaging *Opt. Lett.* **35** 3192–4
[72] Pan B, Xie H and Wang Z 2010 Equivalence of digital image correlation criteria for pattern matching *Appl. Opt.* **49** 5501–9
[73] Zhuo Y, Sun C and Chen J 2014 Adaptive subset offset for systematic error reduction in incremental digital image correlation *Opt. Lasers Eng.* **55** 5–11
[74] Shen B and Paulino G 2011 Direct extraction of cohesive fracture properties from digital image correlation: a hybrid inverse technique *Exp. Mech.* **51** 143–63
[75] Lourakis M and Argyros A 2005 Is Levenberg-Marquardt the most efficient optimization algorithm for implementing bundle adjustment? *Conf. on Int. Conf. on Computer Vision (ICCV) (IEEE)* vol 1 pp 1526–31

[76] Luu L, Wang Z, Vo M, Hoang T and Ma J 2011 Accuracy enhancement of digital image correlation with B-spline interpolation *Opt. Lett.* **36** 3070–2
[77] Wang Z, Nguyen H and Quisberth J 2014 Audio extraction from silent high-speed video using an optical technique *Opt. Eng.* **53** 110502
[78] Kieu H, Pan T, Wang Z, Le M, Nguyen H and Vo M 2014 Accurate 3d shape measurement of multiple separate objects with stereo vision *Meas. Sci. Tech.* **25** 035401
[79] Wang Z, Vo M, Kieu H and Pan T 2014 Automated fast initial guess in digital image correlation *Strain* **50** 28–36
[80] Post D, Han B and Ifju P 1994 *High Sensitivity Moiré: Experimental Analysis for Mechanics and Materials* (Berlin: Springer)